Materials & Design 248 (2024) 113465

Contents lists available at ScienceDirect

Materials & Design

journal homepage: www.elsevier.com/locate/matdes

Hybrid fibre-reinforced cementitious composites with short polyethylene and continue carbon fibres: Influence of roving impregnation on tensile and cracking behaviour

Cesare Signorini *, Ameer H. Ahmed, Marco Liebscher, Jitong Zhao, Thomas Köberle, Viktor Mechtcherine

Institute of Construction Materials, TU Dresden, 01187 Dresden, Germany

ARTICLE INFO

Keywords:
Mineral-bonded composites
Mineral impregnation
Fibres
Carbon textile
LC^3
Bond behaviour

ABSTRACT

Hybrid externally-bonded reinforcements are considered a viable technique for strengthening existing concrete structures. They combine high-performance impregnated textiles with matrices containing dispersed microfibres to foster the ductility and toughness of the composite system. In this paper, the mechanical performance of textile-reinforced strain-hardening cement-based composites (TR-SHCC) is investigated in detail. A novel high-performance inorganic binder based on limestone calcined clay cement (LC^3) is reinforced with both polyethylene (PE) dispersed microfibres and carbon fibre (CF) textiles as continuous biaxial reinforcement. The CF yarns are impregnated by an automated process to improve the monolithic response under uniaxial tensile loading and to ensure high production consistency. Fully inorganic suspensions, i.e., geopolymer and cement-based, are being investigated, as they can provide superior thermal stability compared to traditional polymeric impregnating agents. Interphase adhesion is investigated by single-yarn pull-out tests, microscopy and μCT at various micro scales. On the one hand, the improved adhesion promoted by cement impregnation resulted in the finest and most diffuse crack pattern. Conversely, the strength of the overall composite is mainly governed by the tensile failure of the yarns, irrespective of the bond, and dispersed fibres consistently improve the post-cracking stage and the strength of the hybrid composites.

1. Introduction

The use and the development of fibre- and textile-reinforced cementitious composites has grown rapidly in recent decades as novel materials for new structures and for strengthening existing structures. Their main advantages lie in their excellent and tailorable mechanical performance, combined with high shape flexibility and relatively good durability. In addition, commonly used inorganic binders often have a good chemical affinity with concrete and masonry substrates. Among the technologies currently being investigated, strain-hardening cement-based composite (SHCC) materials, often referred to as engineered cementitious composites (ECC), are extremely attractive [1,2]. Thin-walled structures can be applied to protect against dynamic and extreme loading conditions, on account of their superior damage tolerance entailed by the addition of evenly distributed short fibres in the cement-based mortar. The fracture behaviour of SHCC resembles that of quasi-ductile materials, due to the development of very fine crack patterns that allow a significant energy absorption capacity [3,4]. Furthermore, hybrid reinforcement strategies have been successfully investigated over the last decade, taking advantage of the synergistic combination between SHCC and continuous modular woven textiles. Barhum and Mechtcherine [5] pointed out that the addition of either glass or carbon short fibres to textile-reinforced concrete (TRC) results in a moderate increase in the load-bearing capacity of the composite, associated with a marked delay in the onset of cracking under tensile loading conditions. This effect was traced back to the improved bond established between the multifilament yarn and the surrounding fibre-reinforced cementitious matrix [6]. In general, the energy absorption capacity is significantly improved by the hybrid reinforcement, although the strain capacity is only marginally affected, as it is governed by the brittle nature of the textile, which is generally made of carbon fibres [7]. In fact, the discrete fibres transfer the external load evenly to the textile and the cracks are not concentrated in correspondence with the weft yarns of the textile, but are rather finer and more consistently

* Corresponding author.
E-mail address: cesare.signorini@tu-dresden.de (C. Signorini).

https://doi.org/10.1016/j.matdes.2024.113465
Received 24 June 2024; Received in revised form 21 October 2024; Accepted 12 November 2024
Available online 14 November 2024

distributed along the length of the sample [8], especially for composite elements subjected to dynamic loads [9]. This improved fracture mechanism is also pivotal in improving the long-term performance of the system [10,11]. In general, the aspect ratio of short fibres has a considerable effect on the overall response of the hybrid composite. Zhang et al. [12] showed that when using biaxial textiles, the length of the dispersed fibres should be matched to the grid size opening, as longer fibres may favour the crack-bridging capacity with increasing loading, at the expense of the dispersion quality in the matrix.

As far as reinforcing textiles are concerned, carbon fibres (CF) are the most commonly used for the production of multifilament rovings due to their favourable performance/cost ratio and high resistance to aggressive environments and high temperatures [13,14]. A major drawback is that CF are extremely brittle and do not tolerate abrasion, as they tend to break easily, especially when subjected to pull-out and embedded in matrices containing sharp particles. Moreover, the presence of surface defects that can occur during the spinning process demands the use of polymer sizing and yarn impregnation techniques, to improve durability and stability [15]. Impregnation at the yarn level has the twofold effect of binding filaments together and protecting the fibres from premature failure due to inherent defects and brittleness [16]. Polymeric impregnating agents such as epoxy, polyacrylate, or styrene-butadiene [17,18] are generally used, which generally leads to a remarkable increase in the mechanical behaviour of TRC [19,20], but may compromise the distinctive fire resistance of inorganic composites [17,21–23] and affect the bond to structural substrates [24]. When exposed to high temperatures, epoxy impregnated yarns undergo a rapid degradation process, which negatively affects the interfacial bonding between the phases [25], albeit the chemical composition of the impregnating resin and the shielding effect of the surrounding hydraulic matrix may mitigate or delay these drawbacks to some extent [21]. A possible solution to overcome such limitations associated with organic impregnation is to develop fully inorganic impregnating agents. Some studies report on the development of yarn impregnation techniques rich in amorphous silica, which foster the chemical interaction with cementitious and lime-based matrices [26–28], and open interesting scenarios for the targeted use of more sustainable raw materials featuring high pozzolanic reactivity [29]. In this direction, Schneider et al. [30] have recently developed a novel concept, consisting of using cementitious suspensions to impregnate CF multifilament rovings. This concept was further developed by Liebscher et al. [31] and extended to other kinds of fibre rovings. As a result, rigid composite rods can be produced as reinforcing elements for fine-grained cementitious composites. The impregnation baths are characterised by suspensions of low viscosity and fine particle size distribution to promote the complete impregnation of the inner filaments within the bundles, thus inhibiting poor and scattered frictional failure modes such as the so-called "*telescopic failure*" [32]. The distinctive penetration capacity of impregnating suspensions has also been effectively enhanced by grinding the binder particles [33]. Currently, the development of mineral impregnation of CF rovings has the attractive potential to be incorporated into a fully automated process for rod manufacturing for advanced technological production protocols such as concrete extrusion or 3D printing [34]. The suspension baths can be highly customised, encompassing the opportunity of adopting geopolymer matrices with different precursor sources [29]. The use of geopolymers is a more technologically viable option in terms of environmental impact, cost and efficient industrial production when compared to ordinary Portland cement (OPC) [35], especially for applications with significant material consumption [36]. However, the interaction of geopolymers with cement-based matrices and blends still requires a thorough understanding, despite some encouraging preliminary results have been recently reported in the context of geopolymeric mixes for concrete repair [37].

In this paper, the behaviour of hybrid composites based on a newly developed high-performance limestone calcined clay cement (LC^3) binder strengthened with ultra-high molecular weight polyethylene (UHMWPE) short, dispersed fibres and mineral-impregnated carbon fibre (MCF) continuous yarns assembled into balanced biaxial textiles is investigated for potential use as highly dissipative protective layers for vulnerable concrete elements. Hereafter, this array of composites will be referred to as textile-reinforced strain-hardening limestone calcined clay cement composites (TR-SHLC^3) [38]. The focus is on the comparative assessment of the bond behaviour of geopolymer- and cement-based MCFs and its effect on the tensile response of the composites under quasi-static loading regimes. Common epoxy pre-impregnated carbon fibre reinforcements serve as reference material. Scanning electron microscopy (SEM) implemented with Energy-dispersive X-ray spectroscopy (EDX) and micro-computed tomography (μCT) are conducted to characterise the impregnation quality of the carbon fibre rovings and their interaction with the SHLC^3 matrix. Single-sided yarn pull-out and uniaxial tensile tests are performed to evaluate the mechanical response of the hybrid composites. Finally, the tensile behaviour of TR-SHLC^3 is analysed.

2. Materials and methods

2.1. Raw materials

2.1.1. Carbon fibre yarns and mineral impregnation

The textiles are assembled out of CF rovings purchased from the SGL Group, Germany (SIGRAFIL® C T50-4.4/255 E100), which have been extensively characterised by the authors in previous studies [33]. The features of the carbon filaments and rovings are listed in Table 1.

Two different mineral impregnations are applied to the CF rovings, based on fine cementitious (C) and geopolymer (G) suspensions, respectively. Their compositions, including information on the manufacturers, are given in detail in Table 2 and Table 3.

C suspension consists of a blend of silica fume and two varieties of micro-size cement with different particle size distributions. To achieve an optimal bundle impregnation, the viscosity of the suspension is kept low by the addition of superplasticiser and an increased water/binder ratio of 0.8. As for the G counterpart, metakaolin (MK) powder is used as the aluminosilicate precursor due to its high reactivity and small particle size. The MK grade adopted here features a silica and alumina content of about 53 % and 44 %, respectively. Previous works have dealt with the forming process and the complete characterisation of the MK suitable for mineral impregnation [39], which has a particle size distribution ranging from 0.5 to 15 μm, revealing that the diameter of the fibres, as well as the gaps between adjacent fibres in the bundles, exceeds most of the particles in the suspension (around 80 %).

2.1.2. Hybrid composites

A high-strength matrix containing a commercial grade of OPC, CEM I 52.5R-SR3 (na) from Holcim GmbH, Germany is used in this study. Following the typical LC^3 formulation [40], a 50 wt% cement fraction is replaced by calcined clay (30 wt%), limestone powder (15 wt%), and gypsum (5 wt%), to lessen the clinker factor of the composition. A water/binder ratio of 0.3 and sand/binder ratio of 0.45 are selected in the mix design, along with minor additions of polycarboxylate superplasticiser and viscosity modifying agent (VMA) to adjust the fresh

Table 1
Physical and mechanical properties of the bare yarns and constituent filaments.

Entity	Property	Unit	Value
Filament	Diameter	μm	6.9
	Tensile strength	MPa	4400
	Elastic modulus	GPa	255
	Density	g/cm^3	1.80
	Sizing	—	epoxy, 1 %wt.
Roving	Filaments	No.	50,000
	Yarn count	tex	3450
	A_f	mm^2	1.9

Table 2
Composition of the cement-based (C) suspension for mineral-impregnation of the carbon fibre yarns.

Mixture constituent	Sort / Manufacturer	Density [g/cm^3]	Dosage [g/dm^3]
Micro-cement type 1	Mikrodur R-X, Dyckerhoff GmbH, DE	2.90	345.4
Micro-cement type 2	Mikrodur P-U, Dyckerhoff GmbH, DE	3.10	345.4
Microsilica suspension	Centrilit Fume SX, MC-Bauchemie, DE	1.38	345.4
Plasticiser	MasterRheobuild 30, Master Builders Solutions, DE	1.08	13.0 + 18.1*
Water	—	1.00	493.3

* = Plasticiser is added in two phases (at the beginning and the end of the process).

Table 3
Composition of the geopolymer (G) suspension for mineral-impregnation of the carbon fibre yarns.

Mixture constituent	Sort / Manufacturer	Dosage [g/dm^3]
Metakaolin (MK)	BASF, Ludwigshafen, DE	538
Potassium silicate solution	Geosil® 14517, Wöllner, Ludwigshafen, DE	1000
Superplasticizer	Sapetin D27, Wöllner, Ludwigshafen, DE	62
Potassium silicate activator/MK ratio		1.86

properties of the mix, as detailed in Table 4. The LC^3 mortar is reinforced with UHMWPE (in short, denoted as "PE") dispersed microfibres, at a volume fraction of 2 %. The PE fibres used in this study are characterised by a length and diameter of 6 mm and 18 μm, respectively, and feature a tensile strength and ultimate strain of 2500 MPa and 3.5 %, respectively, according to the manufacturer [41].

2.2. Specimen manufacturing

2.2.1. Samples of the impregnating suspensions

To determine the mechanical properties of the impregnation matrices, five prismatic specimens with dimensions of 10 mm × 10 mm × 60 mm are produced for each composition, namely C and G. The geopolymer matrix is treated at 50℃ for 16 h and additionally cured at 20 °C for 28 days, while the cement matrix is cured at 20 °C for 28 days (with the first 7 days of storage in water). During heating and storage, all G specimens are sealed with polyethylene film to minimise water evaporation.

Table 4
Mix design of the SHLC^3 matrix.

Constituent	Role	Sort / Manufacturer	Dosage [g/dm^3]
OPC	Binder	CEM I 52.5R-SR3 (na), Holcim, DE	599
Calcined clay		Liapor, DE	379
Limestone powder		Saxodol 90 LE, sh-minerals, DE	190
Calcium sulphate		Hemihydrate, Grüssing, DE	30
Quartz sand	Inert aggregates	BCS 413, Strobel, DE	536
Fibres	Reinforcement	UHMWPE SK60, Dyneema®, NL	20
Superplasticizer	Admixtures	Glenium ACE 460, BASF, DE	11
VMA		MasterMatrix UW 420, Master Builders Solution, DE	2
Water			359

2.2.2. Yarn impregnation and textile production

The G bath is prepared by mixing potassium silicate activator, MK and superplasticiser. An IKA® T50 digital ULTRA TURAXX® high-speed disperser at a rotational speed of 7000 rpm for 7 min is used to stir the suspension. To prepare the C suspension, micro-silica is first mixed with water and a part of superplasticiser. After one minute of stirring, the micro-cement powders are progressively incorporated under continuous stirring to obtain a homogeneous slurry. Eventually, the rest of the plasticiser batch is added and further homogenised by means of an intensive blender (T50, digital Ultra-Turrax®) at a rotational speed of 7000 rpm.

The mineral-impregnated carbon fibre (MCF) yarn is produced using an automated continuous pultrusion process as shown in Fig. 1a. The CF yarn is drawn by winding it onto a large hexagonal motor-driven wheel under constant tension and passed through three yarn guides, a motor-driven kiss-coater and a suspension bath containing a Foulard five-roller system. The draw speed is set at 6 m/min. The yarn is deflected five times with a 4.2 cm roller to ensure a thorough impregnation. Eventually, the freshly pultruded yarns are shaped by two conical nozzles with an internal diameter of 4.1 mm and placed on the wheel without any contact, controlled by an automatic linear unit. After impregnation, the fresh MCFs are immediately deposited in the desired mesh structure. During processing, the MCF yarns are constantly stretched and aligned on a wooden plate with cylindrical pins fixed to it (see Fig. 1b). The resulting textile structure has a square shape with a side of 750 mm and a grid size of 30 mm, dictated by the distance of each pair of adjacent pins. The individual yarns of the textile reinforcement are then connected together with a hot melt adhesive using a hot glue gun (for the C-MCF) and with the same G suspension (for the G-MCF) to ensure the necessary robustness of the stitching between orthogonal yarn elements. C-MCF textiles are left to hydrate for 1 day at laboratory conditions and then stored in water for additional 7 days. The curing process is completed with a further 21 days in a climate chamber at 20 °C. G-MCF textiles are cured at 50 °C for 16 h and then stored in water for 7 days, with the water in the bath refreshed every 24 h to remove residual alkali ionic species. The textiles are then cut into the desired pieces, before the TR-SHCC plates are produced. A commercially available epoxy-impregnated carbon textile (GRID Q85/85-CCE-21, Solidian, Germany) is also considered as a comparison term. Fig. 2 shows a visual comparison of the textiles.

The mechanical properties, i.e., tensile strength, modulus of elasticity and bending strength, of the impregnated yarns are assessed in previous works [31,39], and results are summarised in Table 5. The difference in tensile strength is mainly due to the different inherent properties of the CFs for the commercial epoxy-impregnated textile, which may differ from those of the yarns produced in-house. In addition, during the impregnation process, some of the filaments may be damaged by abrasion from the particles in the mineral suspension.

2.2.3. Hybrid composite preparation

The uniaxial tensile tests are performed on slender prismatic plates, as shown in Fig. 3, featuring width and length of 100 mm and 700 mm, respectively. The 200 mm long region at the edges of the specimen serves as the clamping region and textile anchorage zones and is reinforced with additional textile layers (highlighted in red in Fig. 3). This provision is adopted to avoid premature failure when lateral restraint is applied during testing when a rigid gripping configuration is used [10,42]. The gauge length, L_g, of the rectangular plates is set at 300 mm. The total cross section of the specimen is $A_{tot} = 2000mm^2$. The geometry of the TR-SHLC^3 samples as well as the gripping system were designed to meet the minimum requirements of the RILEM TC 232-TDT recommendations for TRC [43]. Four identical specimens are produced and tested for each parametric configuration. Each plate accommodates 4

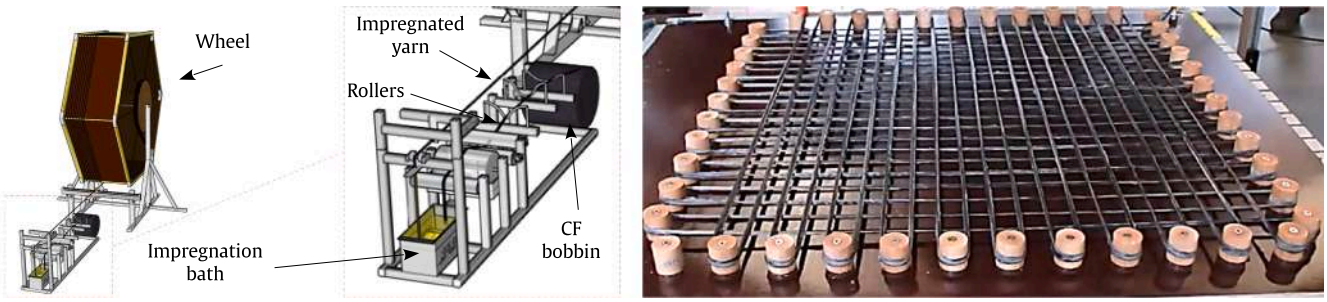

(a) (b)

Fig. 1. Scheme of the continuous and automated processing line for MCF yarns (a) and curing phase in their final mesh structure (b).

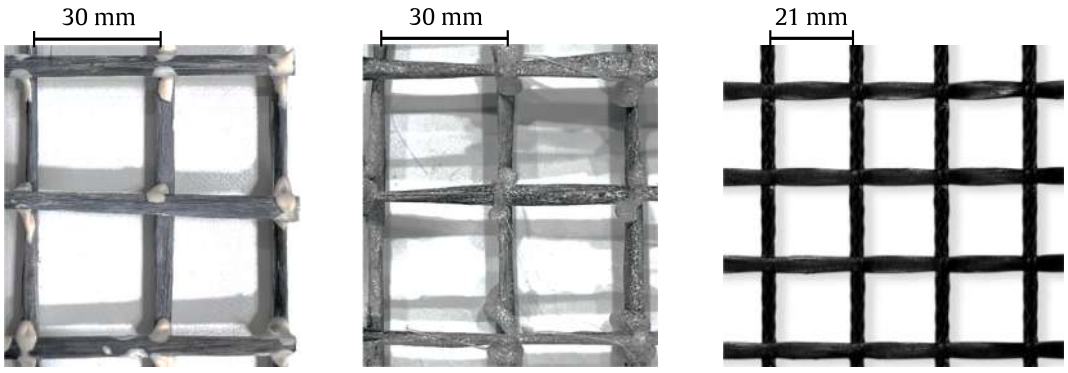

(a) G-MCF (b) C-MCF (c) E-CF (reference)

Fig. 2. MCF carbon yarns assembled as bi-axial balanced textiles, and commercial epoxy-coated textile as a reference.

Table 5
Mechanical properties of impregnated carbon yarns (properties of E-CF are given by the manufacturer). In parentheses the coefficient of variation (CoV) is reported.

Property	unit	C-MCF	G-MCF	E-CF
Tensile strength	MPa	2250 (±7.6 %)	2103 (±4.9 %)	3300
Elastic Modulus	GPa	225 (±2.7 %)	246 (±3.5 %)	250

warp yarns for the mineral-impregnated textiles (cross-sectional area of carbon fibres, $A_f = 7.6\ mm^2$, geometric reinforcement ratio, $\rho_f = \frac{A_f}{A_{tot}} = 0.38\%$) and 5 warp yarns for commercial the epoxy-impregnated textile ($A_f = 9.1\ mm^2$, $\rho_f = 0.45\ \%$) considered as reference.

In order to directly measure the matrix-yarn interface parameters, single-sided yarn pull-out tests are conducted. The edges of a single 220 mm long CF yarn are embedded in two blocks made of the SHLC^3 matrix separated by 120 mm. The smaller block (50 × 80 × 80 mm^3), regarded as the "*test block*", serves for accommodating the yarn for the embedded length of 10 mm. The larger block (90 × 80 × 80 mm^3), regarded to as the "*anchoring block*", provides a much larger anchoring zone for the yarn at the opposite end to facilitate debonding and pull-out from the test block. Fig. 3b shows the geometric configuration of the single-sided yarn pull-out specimen [30]. The samples for the uniaxial tension tests are cast using a layer-by-layer wet lay-up technique, whereas the blocks for the yarn pull-out test are produced by gently pouring the matrix around the yarn and jolting it slightly.

For the uniaxial tensile tests, customised lubricated moulds are half filled with the SHLC^3 matrix, then textiles are laid on the matrix and gently pressed, to locate them in the centre of the cross section using a thickness marker. The final layer of the matrix is then applied, levelled and smoothed with a trowel. In the case of the pull-out specimens, a channel ensures that the yarn is perfectly centred within the two blocks. Once the specimens are cast, the moulds are wrapped tightly in plastic covers for 24 h to allow moist-curing to take place. The specimens are then demoulded, sealed in plastic bags, and stored in a climatic chamber at a temperature of 20 °C (±10 %) for a further 27 days. The textile reinforcement ratio is 0.42 % for MCF and 0.57 % for epoxy CF.

2.3. Test methods

2.3.1. Analytical investigation techniques

The MCF yarns and composite samples are examined using a variety of techniques. Optical microscopy (Video microscope VHX 6000, Keyence, Germany) is adopted to investigate the portion of the yarns extracted during the pull-out tests. Scanning electron microscopy (SEM, Quanta 250 FEG, FEI, The Netherlands) is also used to analyse the bare yarns, as well as drill cores with 20 mm diameter retrieved from the anchoring blocks of the pull-out specimens with the yarn in the centre. The aim of the latter investigation is to analyse the undisturbed portion of the specimens and highlight the inherent quality of the bond. Both sorts of sample are carefully placed in a small cylindrical mould in a vertical position before being impregnated with epoxy resin. The top surface is then cut and polished with oil and diamond paste to reveal the cross-section. Backscattered electron imaging (BSE), in combination with Energy Dispersive X-ray spectroscopy (EDX, Quantax 400, Bruker, Germany), is chosen to highlight the different chemical elements in the samples.

A micro-computed tomography (μCT) scanner CT-XPRESS from ProCon X-Ray, Germany, equipped with a high productivity 65 W X-ray tube and a high resolution flat panel detector is used to investigate the yarn-to-SHLC^3 bond on the aforementioned drill cores. Scanning conditions are 100 kV and 66 μA with 1441 projections. Each scan lasts approximately 1 h at a sampling rate of 0.5 fps. The scans are then iteratively reconstructed using the X-AID software (MITOS, Germany).

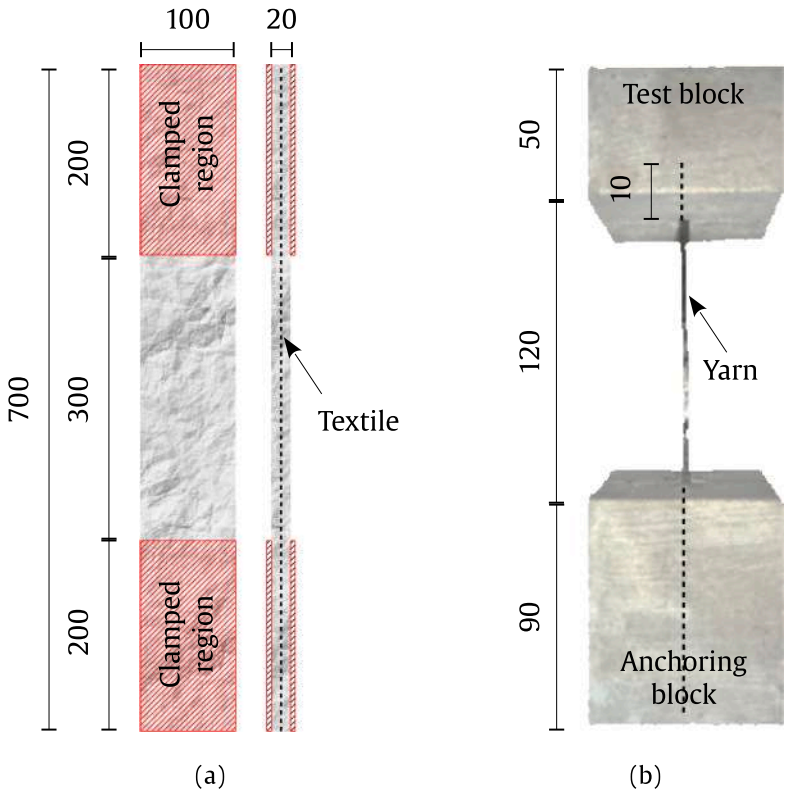

Fig. 3. Geometry of (a) slender-plate specimens and (b) single-sided pull-out tests. The highlighted region represents the clamping area and textile anchorage zones, while the force is applied along the vertical direction. Dimensions are in mm.

2.3.2. *Mechanical properties of impregnating suspensions and hybrid composites*

To characterise the mechanical performance of the G and C impregnating suspensions, three-point-bending tests are performed on $10 \times 10 \times 60$ mm^3 prisms at a loading rate of 1 mm/min using a universal testing machine Z1445 (Zwick Roell, Germany). Compressive tests are also carried out on the five pairs of halves remaining after the bending tests using the same test set-up, with a loading area of 30 mm.

The uniaxial tension tests are carried out in a servo-hydraulic universal testing 8501 (Instron, USA) machine in a displacement controlled regime. The test speed is set at 0.05 mm/s. A set of rigid hydraulic clamping plates with controllable pressure is used to grip the specimens, which transfer the load to the specimen by friction. The applied pressure in the clamping region is about 10 MPa, which was sufficient to prevent the specimens from slipping and crushing [18], as recommended by the RILEM TC-232 guidelines [43]. This setup allows for a more uniform stress distribution over the specimen cross-section and an accurate determination of the constitutive response of the hybrid composite in tension [44]. The mechanical setup is coupled to an optical system consisting of two cameras and a high intensity blue light source (GOM GmbH, ZEISS Group, Germany) for Digital Image Correlation (DIC) analysis. The frequency of the cameras is set at 2 Hz. Prior to mounting the specimens in the test setup, the gauge length is sprayed with white paint followed by the application of a high density stochastic pattern of fine black dots. The recorded images from the test are analysed in ARAMIS (GOM GmbH, ZEISS Group, Germany) at the end of each test to evaluate strains, crack widths, and crack densities. The load signal from the testing machine is transferred to the ARAMIS software, which is synchronised in real time with the frequency of the cameras. To compute strains, two virtual callipers are constructed on each side of the gauge length in the ARAMIS software and the elongation is monitored throughout the whole test duration. Similar callipers are placed at each crack within the gauge length for crack width analysis.

Single yarn pull-out tests are performed in the same universal testing machine. The diameter of each yarn is measured prior to testing and the bond strength is computed by dividing the measured force F by the lateral surface of the yarn. Further details and sketches of the test setup are given in a previous publication [30].

3. Results and discussion

3.1. *Suspensions characterisation*

Table 6 reports on the flexural and compressive strengths of the two inorganic suspensions used as impregnating agents for MCF in this study. It is worth noting that suspension G features a moderate compressive strength, whereas suspension C has a poor mechanical performance. This is due to the higher water content and, in particular, the higher dosage of superplasticiser [45], which exceeds the recommended range of 0.1–3.6 % of cement weight, according to the manufacturer's guidelines. These measures were necessary to achieve the appropriate viscosity to allow full impregnation of the multifilament yarns.

3.2. *Impregnation quality and bond behaviour*

Fig. 4 shows the SEM-BSE images illustrating the cross section of the MCF yarns, after complete curing of the impregnating suspension and before embedding in the SHLC[3] matrix, compared to as-received

Table 6
Mechanical properties of the impregnating agents (standard deviation in brackets).

Suspension	Flexural strength	Compressive strength
	[MPa]	[MPa]
G	8.0 (±1.5)	36.9 (±5.9)
C	0.8 (±0.1)	9.1 (±3.0)

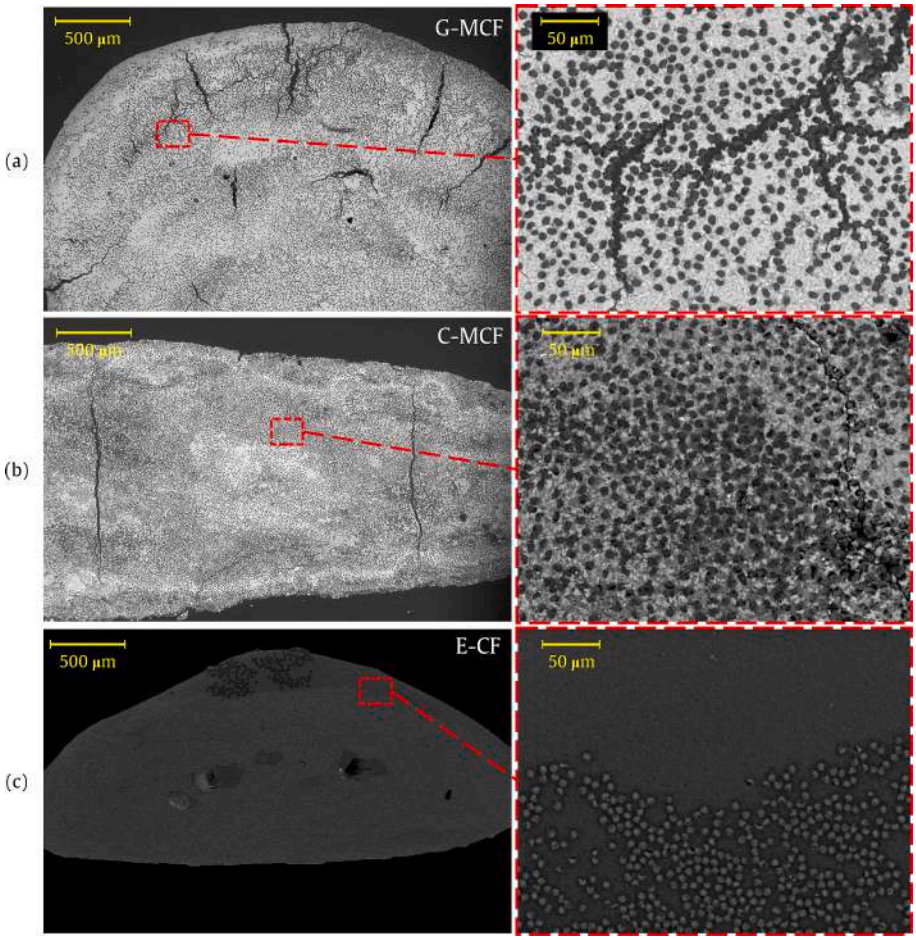

Fig. 4. SEM images investigating the impregnation of carbon yarns by mineral-based suspensions (a-b). Epoxy-impregnated commercial yarns are shown as a comparison term (contrast and brightness are adjusted for better visibility) (c).

commercial epoxy yarns. In the images, the darker dots identify the individual carbon filaments or cracks, while the surrounding matrix is visible in lighter grey. Most of the internal cracks in the MCF yarns can be attributed to the polishing phase during specimen preparation for SEM analysis, combined with the brittle nature and low strength of the impregnation, especially for C-MCF.

The impregnation of the commercial yarns, which are produced by an industrial process using epoxy as the binding agent, is characterised by a uniform embedding of the individual filaments. However, there are some discontinuities in the impregnation of the yarn core. In some cases, the E-CF yarn is surrounded by a thick outer layer of epoxy, in which only a few filaments are embedded. Polymer fibres used as stitching elements are visible in the upper part of the yarn as they are thicker than the carbon fibres. The darker, wider areas in the cross section of inlets (a) and (b) denote defects in the impregnation of the MCF. The quality of the mineral impregnation appears to be uniform throughout the cross section of the yarn. Indeed, CFs are treated with epoxy sizing during spinning and possess relatively good water wettability compared to other common sizing resins such as thermoplastic [46]. The C impregnating medium consists of visibly larger aggregates compared to the G one. However, the fineness of both suspensions is sufficient to penetrate deeply into the yarn bundles.

Fig. 5 shows the elemental EDX spectra for MCF yarns, with particular emphasis on calcium (Ca), silicon (Si) and aluminium (Al). As expected, silicon is predominantly and evenly detected in G-MCF, together with aluminium and oxygen (not shown here), in the form of silica and

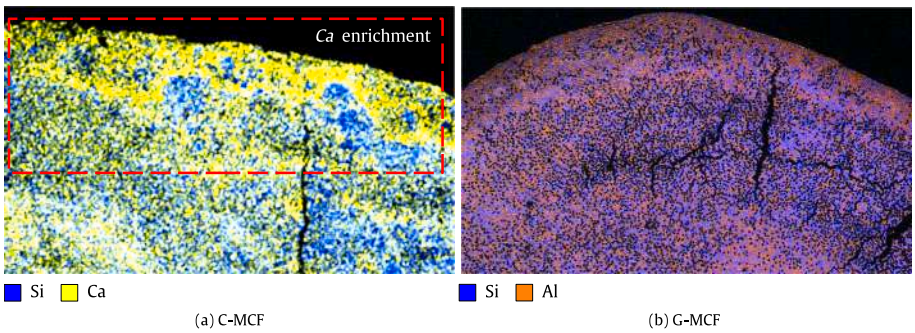

Fig. 5. EDX elemental colour maps showing the distribution of calcium (Ca), silicon (Si) and aluminium (Al) within the cross-section of the mineral-impregnated yarns.

alumina. C-MCF exhibits both calcium and silicon as reaction products of cement hydration. However, an enrichment of calcium (Ca) is observed in the outer region of the yarn cross-section, which can be attributed to the larger particle sizes of the cementitious particles compared to the used silica. The high number of CF filaments (50,000), having an average diameter of 7 μm each, acts as a filter against particle migration. Hence, the small sized silica particles are abler to penetrate the roving core yielding in the slight inhomogeneous elemental distribution over the MCF cross-section.

Extending the SEM analysis to the composite level, the appearance of the interphase transition zone (ITZ) between the MCF yarn and the surrounding SHLC^3 matrix is shown in Fig. 6 and Fig. 7 for G-MCF and C-MCF, respectively. Specimens are taken from the core of the anchoring blocks and therefore show the undisturbed appearance of the yarn-matrix interphase.

Inlets (a) provide a global view of the yarn, while inlets (b) focus specifically on the interface using the secondary electron detector. For C-MCF, EDX elemental colour maps are also shown in inlet (c). Some microcracks, likely due to sample polishing, can be detected passing through the interface between MCFs and the SHLC^3 phase, as well as in the yarn core. Again, the elemental mappings for C-MCF highlight the presence of an enrichment of calcium concentrated at the interface, in combination with an increased carbon signal, which stands out against the black background. This additional layer, which formed rapidly during the curing period of the C suspension, developed before the casting of the hybrid specimens, although it appears to be more pronounced at this stage. It possesses a thickness of about 3–5 μm and consistently follows the shape of the yarn cross-section (see Fig. 7b-c). In the case of the G-MCF yarn, a clear distinction between the impregnated yarn portion and the LC^3-based matrix is evident in SEM micrographs. The matrix is easily identifiable in the upper part of Fig. 6b, where quartz sand and limestone particles are visible, whereas the G impregnation is visible in the lower part, characterised by a more uniform texture.

Fig. 8 shows the magnification of the ITZ for the two sorts of MCF compared to the E-CF reference. Despite these comparative images cannot give a conclusive indication of the chemical interaction at the ITZ, it can be noted that G-MCF unveils a well-defined distinction between the two phases, which appear to be simply adjacent and not interconnected. In fact, a very thin crack is visible throughout the whole boundary. On the one hand it should be noted, that the G-MCF possess a very smooth surface and low porosity which may reduce the wettability of the fresh mortar during casting. On the other, this outcome is also in line with a recent study by Wang et al. [47] in the field of geopolymer repair mortars on concrete substrates. They pointed out that a better bond is achieved by using repair formulations rich in calcium, which are prone to generate more secondary hydration products across the ITZ than repair mortars with a low calcium content. In the case of the G formulation presented here, silica is the dominant phase and calcium content is negligible (as confirmed by the EDX elemental maps in Fig. 5b). Silva et al. [25] found out a certain incompatibility between concrete and G-MCF as well. Similar to the G-MCF observations, the E-CF counterpart has extremely dense impregnation and shows a fine crack propagating along the ITZ and in some cases deviating into the inorganic matrix. Conversely, the interface between the embedding matrix and the C-MCF yarn appears to be mostly interconnected, likely as a consequence of the chemical affinity of the two phases as well as MCF porosity allowing a certain penetration of the freshly applied mortar.

Further analysis of the ITZ is provided by μCT scans, performed on cylindrical cores drilled in the vicinity of the yarn. The scans in Fig. 9 display the longitudinal sections for C-MCF and G-MCF, compared to their E-CF counterpart. It should be noted that with this kind of non-destructive technique, the yarn-to-SHLC^3 interface is not disturbed by any polishing or grinding treatment and thus reflects the actual bond state [48]. Interestingly, the texture of the portion of the SHLC^3 matrix immediately adjacent to the yarn appears to be densely packed, as far as the C-MCF yarn is concerned. Conversely, no analogous phenomenon is visible for G-MCF, whose interface presents a porosity similar to that of the outer SHLC^3 matrix (pores are identifiable as black dots). Moreover, a wide longitudinal crack visible on the right side of the yarn provides evidence of a weaker interaction established with the surrounding matrix. This phenomenon was also reported by Silva et al. [25] and explained by a potential alkali–silica reaction (ASR) due to residual alkaline cations from the G suspension. Those may induce a damage of the ITZ and hence impair the loading bearing capacity. It is worth noting that a longitudinal crack is also partially initiated on the top right of the C-MCF counterpart. In this case, however, it occurs outside the ITZ, but rather in the matrix [49].

The results of single-sided yarn pull-out tests in terms of shear stress vs slip curves are presented in Fig. 10. Shear stress was computed by normalising the measured load to the average lateral surface of each yarn ($\pi d_y L_e$), where d_y is the average diameter of the yarn and L_e is the embedded length. Pull-out curves reveal an initial steep straight branch, reflecting the linear regime of the bond law [50]. E-CF samples show a significantly more compliant trend at this stage when compared to both MCF counterparts. A diffuse microcracking pattern is then likely to be triggered in the interphase due to high shear extents, reducing the stiffness of the bond curve until the peak stress is attained. Once the peak stress is reached, yarn extraction initiates, and the response is governed by pure friction. The peak value is considered the bond strength (τ_{max}) and comprises the sum of the chemical and physical bond uniformly averaged over the entire embedded length. Due to the high stiffness of CF, the axial deformation of the free yarn is minimal during the first stage. In the case of MCF yarns, an abrupt stress drop is observed at the threshold between the debonding and the pull-out stages, defining the so-called frictional bond strength (τ_{fr}), i.e. the residual stress withstood by frictional forces after complete yarn debonding [51]. The magnitude of this stress drop is an indicator of the quality of the chemical bond [52], and in the case of E-CF is indeed barely perceivable, a clear indication of the poor chemical interaction with the cementitious matrix. On the contrary, sharp stress drops are generally associated with a strong

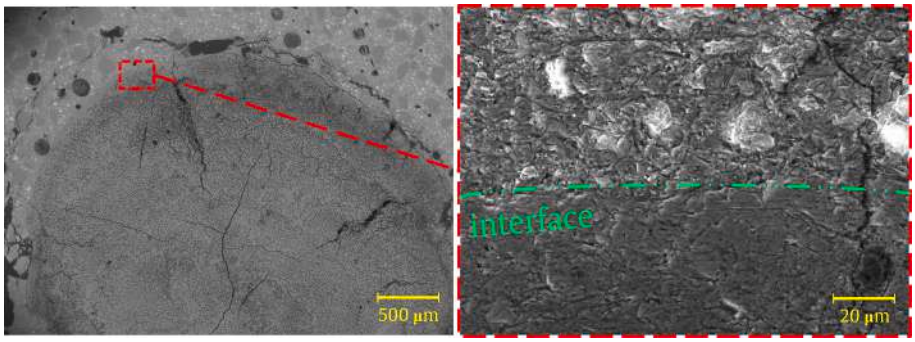

Fig. 6. SEM images investigating the interface between geopolymer impregnated (G-MCF) yarns and the surrounding matrix after complete curing.

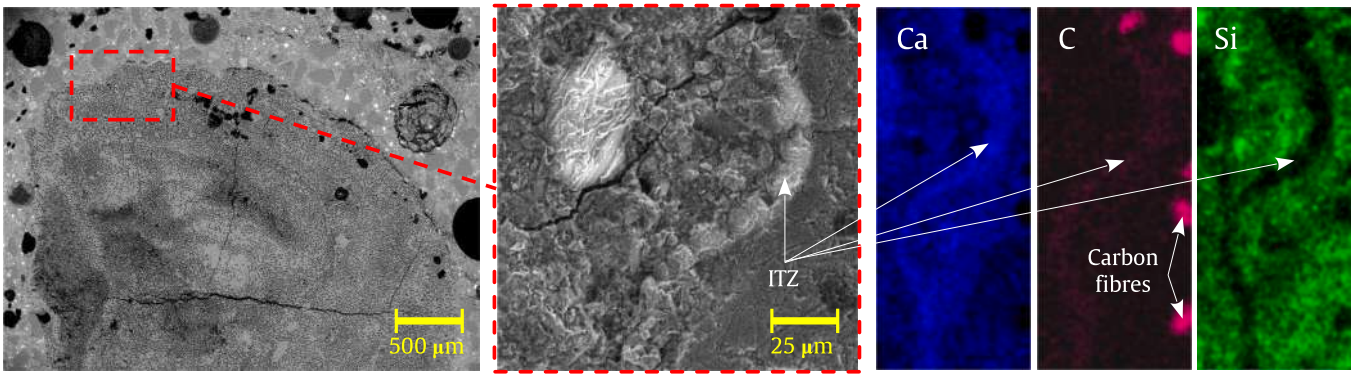

(a) Wide view (b) Magnification at the ITZ (c) EDX colour maps

Fig. 7. SEM images investigating the ITZ between cement impregnated (C-MCF) yarns and the surrounding matrix after complete curing.

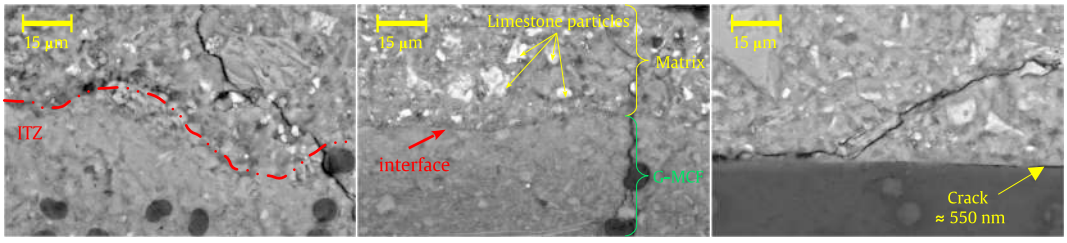

(a) C-MCF (b) G-MCF (c) E-CF

Fig. 8. SEM-photo at high magnification (BSE mode) detail of the ITZs of the two MCF.

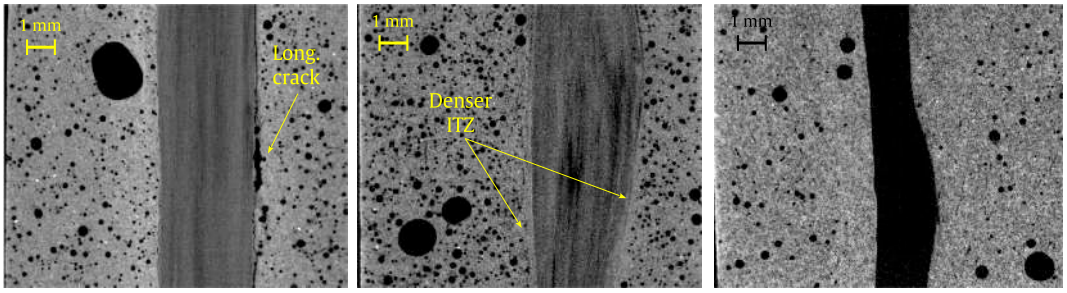

(a) C-MCF (b) G-MCF (c) E-CF

Fig. 9. µCT scanning of composite cores.

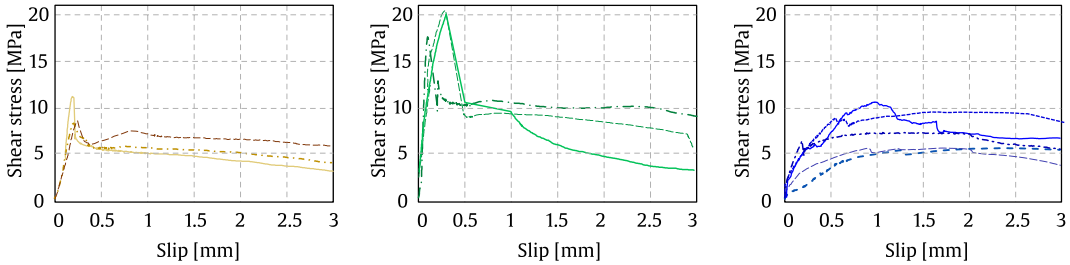

(a) G-MCF (b) C-MCF (c) E-CF

Fig. 10. Single-yarn pull-out test results for MCF embedded into SHLC[3] matrix.

chemical bond. During yarn extraction, generally decreasing residual stresses due to friction can be observed. The curves show that frictional bond for C-MCF is initially higher than that for G-MCF. However, this effect tends to flatten out at slip values higher than 2 mm, when the interphase zone is fully compromised regardless of the impregnation material. The E-CF counterpart shows a distinct trend, highlighting a certain increase in the residual stress up to higher slip values, followed by a milder decay, further indicating the prominent or even exclusive role of the frictional bond or E-CF samples, counterbalancing the poor or absent chemical interaction.

For comparison, bar-charts of the mean values for peak and frictional bond strength and energy values are shown in Fig. 11, including the statistical variation of the results by standard deviation intervals. The scatter of the data is moderate due to the limited embedded length, which on the one hand prevents the possibility of the bond force exceeding the tensile force, resulting in an undesired failure mode, but on the other hand could emphasise the presence of manufacturing defects. Nevertheless, the accuracy of the results can be considered in line with similar investigations [33,53]. Fig. 11b compares the total absorbed energy (analogous to W_{total} proposed by Silva et al. [25]) due to adhesion and friction, computed as the area under the stress-slip diagrams up to 4.5 mm of yarn extraction (expressed in MPa mm), while Fig. 11c estimates the chemical debonding energy (expressed in J/m^2) according to the Equation (1), adapted from Peled et al. [51], with E_y values taken from Table 5.

$$G_d = \frac{2L_e^2(\tau_{max} - \tau_{fr})^2}{E_y d_y} \quad (1)$$

In Equation (1), L_e is the embedded length, d_y is the diameter of the yarn, τ_{max} and τ_{fr} are the maximum and the residual tangential stresses, respectively. The latter is of mere frictional (subscript "*fr*") nature and is obtained as the shear stress after complete debonding [51]. As envisaged from the microscopic and tomographic analyses, varying the impregnating agent for the CF yarns has a profound effect on bond behaviour. Specifically, the C impregnation outperforms the G impregnation by 87 % in terms of bond strength, i.e., the resistance to yarn debonding from the surrounding SHLC^3, and consistently by 51 % in terms of total debonding and pull-out work. Remarkably, a significant gap is achieved in terms of chemical debonding energy, which is about 7.5 times higher for C-impregnated yarns when compared to its counterpart, thereby proving the affinity between the cement-based yarn impregnation and the LC^3 matrix. In fact, while the total absorbed energy mainly encompasses the contribution of friction, which characterises most of the development of the stress-slip curve, G_d provides the distinct quantification of the quality of the chemical interaction between the yarn – considered as a monolithic entity – and the surrounding matrix.

The optical microscopy images in Fig. 12 show the magnification of the portion of the yarns originally embedded in the SHLC^3 matrix after being extracted during the pull-out tests. In general, in both cases, patches of matrix are bonded to the yarns. However, the G impregnation is more prone to cracking and delamination from the filaments than the C impregnation due to its much higher modulus and more brittle behaviour. In addition, the CFs interact better with the cementitious matrix, as can be seen in the papers by Zhao et al. [39] and Li et al. [54], where microscopic analysis shows more matrix residuals on EP-sized CFs with C-based suspension.

3.3. Tensile testing

3.3.1. SHLC^3 matrix

Fig. 13 shows the stress–strain response of the SHLC^3 matrix, which was taken as a baseline to evaluate the mechanical response of the TR-SHLC^3 hybrid composites. The response is consistent with previous investigations combining the LC^3 matrix and PE fibres [9], featuring a tensile strength of 4.0 MPa (±5%) and a strain capacity of 0.96 % (CoV of 0.06 %). This behaviour is associated with the development of multiple cracks with an average width and spacing of 131 μm and 12 mm, respectively, at the onset of the strain-softening stage.

3.3.2. TR-SHLC^3 composites

Charts in Fig. 14 plot the strength curves obtained from tensile tests of prismatic plates performed on hybrid composites containing SHLC^3 matrix and impregnated textiles. The common approach followed for TRC is used to display the stress values on the *y*-axis, which are obtained by normalising the applied force to the cross-sectional area of the warp textile yarns only, assuming that, after crack saturation is reached, the load-bearing action of the composite is carried solely by the textile [55].

However, unlike conventional TRC, cracks in hybrid composites are not stress-free due to the crack bridging exerted by short fibres. Adopting this approach, it is therefore possible to estimate the contribution of the dispersed fibres to the mechanical response of hybrid composites.

The strength curves for the hybrid TR-SHLC^3 specimens follow a distinct bilinear trend, differently to what is generally found for TRC composites with good textile-matrix bond, which instead often show a trilinear behaviour, including an intermediate flat branch encompassing crack formation to saturation [56,57]. In addition, a trilinear behaviour would also be expected for TRC when a rigid clamping setup is adopted [58]. However, in the present case, where a rigid clamping system is indeed adopted, the bilinear behaviour can be attributed to (i) the presence of a pseudo-ductile matrix, i.e. SHLC^3, which can effectively and uniformly transfer the external load through the crack-bridging attitude of the PE fibres and regulate the energy release during the cracking phase by smoothly shifting the load-bearing capacity from the matrix to the textile. In fact, in the proximity of the weft yarns of the textile, where the cross section is obviously weakened, the formation of a fine pattern is achieved rather than sharp transversal cracks associated with severe energy releases [18]. Secondly, (ii) the high quality of the bond between yarns (especially MCF) and the surrounding SHLC^3 matrix documented in the previous sections could explain a certain strain-hardening during the whole crack formation process, smoothly merging the two main stages, i.e. uncracked and post-cracking stages, into a bilinear curve, as also asserted by Arboleda et al. [59] and Butler et al. [60].

3.3.2.1. Stiffness in the uncracked and post-cracking states. The slopes of the curves over the two stages are evaluated according to the method proposed by the ICC AC 434 [61] and Arboleda et al. [62], as the secant straight lines passing through the coordinate origin and 10 % of the peak load (*uncracked* stage), and through 60 % and 90 % of the peak load (*post-cracked* stage), see Equations (2). The intersection of the two lines is conventionally regarded to as the first cracking strength [43,55,61–63].

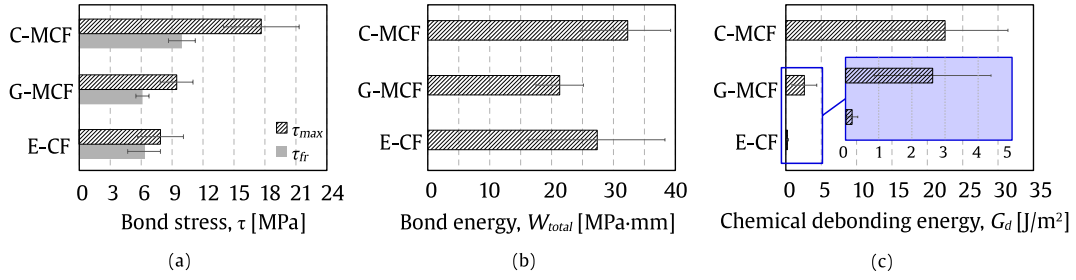

Fig. 11. Mean strength and energy values for MCF embedded into SHLC^3 matrix.

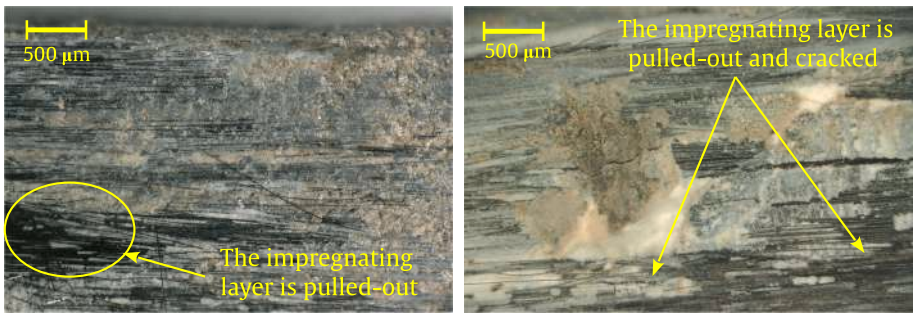

(a) C-MCF (b) G-MCF

Fig. 12. Video microscope photo showing the appearance of the pulled-out portions of MCF yarns after pull-out tests. The inner portions of the embedded length are on the left-hand side of the pictures.

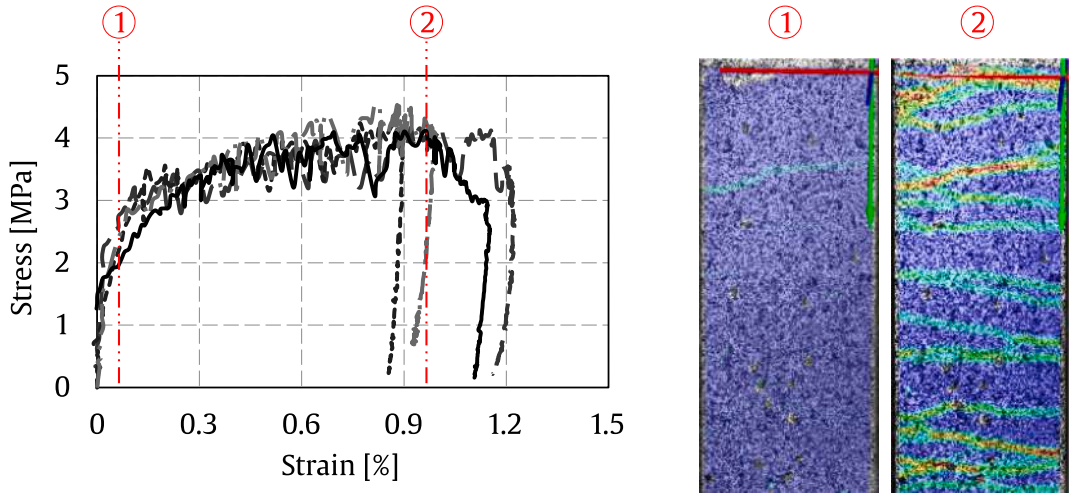

Fig. 13. Strength curves for tensile tests conducted on SHLC[3] matrix samples. Load values have been normalised to the entire cross section of the laminate. The crack pattern (colour map of longitudinal strains) is shown at the formation of the first crack (1) and at the onset of the softening branch (2) for a typical sample.

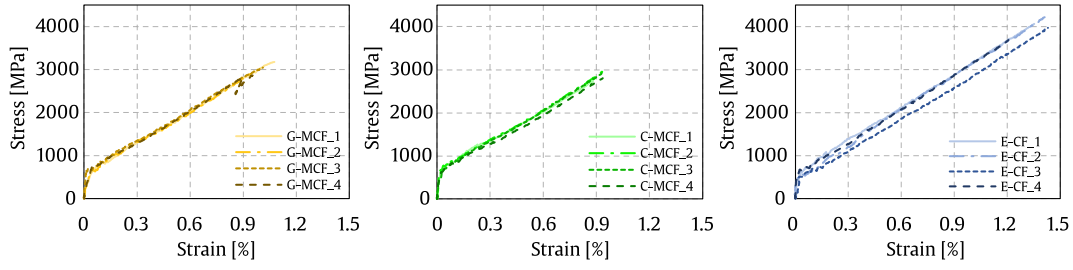

(a) G-MCF (b) C-MCF (c) E-CF

Fig. 14. Strength curves for tensile tests. Load values have been normalised to the net area of fibres in the yarns (A_f).

$$E_1^m = \frac{\sigma^m_{0.1f_{f,max}}}{\varepsilon_{0.1f_{f,max}}} = \frac{P_{0.1f_{f,max}}}{A_{tot}\,\varepsilon_{0.1f_{f,max}}}$$
$$E_2^f = \frac{\sigma^f_{0.9f_{f,max}} - \sigma^f_{0.6f_{f,max}}}{\varepsilon_{0.9f_{f,max}} - \varepsilon_{0.6f_{f,max}}} = \frac{P_{0.9f_{f,max}} - P_{0.6f_{f,max}}}{A_f\left(\varepsilon_{0.9f_{f,max}} - \varepsilon_{0.6f_{f,max}}\right)} \quad (2)$$

Again, as is common practice for TRC, two different approaches to calculating the two slopes are considered, based on the very different mechanical responses of the specimen over the two stages.

- The *uncracked modulus* E_1^m (with superscript "*m*", standing for "matrix") is obtained normalising the measured force at 10 % of the peak force, $P_{0.1ff,\max}$, to the entire cross section of the specimen (A_{tot}), as the undamaged SHLC[3] matrix and textile contribute synergistically to the stiffness of the system, i.e., $\sigma^m_{0.1f_{f,max}} = \frac{P_{0.1f_{f,max}}}{A_{tot}}$.
- The *post-cracking modulus* $E_2{}^f$ (superscript "*f*", standing for carbon "*fibres*"), sometimes referred to as "*strain-hardening modulus*" as it does not reflect an intrinsic material property but is rather an indicator of damage [11], is instead obtained by normalising the measured force at 60 % and 90 % of the peak force, $P_{0.6ff,\max}$ and $P_{0.9ff,\max}$, respectively, to the sole cross-sectional area of the textile, A_f, i.e. $\sigma_i^f = \frac{P_i}{A_f}$, with i being either 60 % or 90 % of the peak load.

In fact, in conventional TRC, the brittle matrix is completely cracked

and does not contribute to the overall stiffness of the composite. The fact that the stiffness values of $E_2{}^f$ are sensibly higher than that of the corresponding E_1^m is due to these two different normalisation approaches.

A schematic representation of the approach to calculating the moduli and the normalisation is illustrated in Fig. 15, which shows a typical experimental P-ε (load vs. engineering strain) curve and the two secant lines that conventionally represent the slopes.

An initial elastic branch is observed, representing the uncracked regime of the composite. At this initial stage there is unlikely to be any deformation mismatch (i.e. slip) between the yarn and matrix and the compatibility of the phases, matrix, *m,* and fibre yarns, *f*, is maintained ($\varepsilon_m = \varepsilon_f = \varepsilon_{TR-SHLC^3}$). As a result, the entire cross section of the specimen contributes fully to the strength and stiffness. Due to the limited reinforcement ratio of the internal reinforcement ($\rho_f = \frac{A_f}{A_{tot}} = 0.38\% - 0.45\%$), the external load is mainly balanced by the SHLC^3 matrix.

A very narrow and smooth transition is then observed at the initial cracking stage of the SHLC^3 matrix, heralding the second pseudo-linear stage, characterised by the presence of diffuse matrix cracking, with the internal textile and the bridging PE fibres bearing most of the external load. The slope of the strain-hardening branch (post-cracking stage) is significantly reduced than that of the uncracked stage, as the matrix is progressively damaged. Specifically, if the same normalisation as that of E_1^m is considered, post-cracking moduli turn out to be ranging from 0.93 GPa of the MCF specimens to 1.18 GPa of the reference E-CF specimens (retaining only a small fraction of 6–7 % compared to the corresponding uncracked moduli). Ultimately, the failure is consistently attained by tensile failure of the yarns within the gauge length of the prismatic specimens. Fig. 16 compares the moduli E_1^m and $E_2{}^f$ and the first cracking strength of the two TR-SHLC^{3}s, including MCF textiles, compared with the E-CF counterpart as a reference.

As far as the uncracked modulus and first cracking strength are concerned, moderate uncertainties are expected owing to the scattered nature and localisation of internal defects. However, the values are close to those of the plain SHLC^3 matrix [64], which confirm the limited load share undertaken by the textile over this mild loading stage. Although the scattering does not allow a clear distinction between the mean values, the slightly lower values obtained for the composites with MCF with respect to the E-CF counterpart in terms of uncracked modulus and first crack stress can be attributed to the thicker weft/warp joints of MCF due to the manufacturing and assembly process, which reduce the SHLC^3 cross-section much more than the commercial textile.

On the other hand, while analysing the modulus in the post-cracking state $E_2{}^f$, with the normalisation to the fabric cross-sectional area introduced in Equation (2) based on the guidelines for conventional TRC with brittle matrix [43], it can be observed that is close to that of CF yarns, attesting to the prominent role played by the textile in the determination of the stiffness at the post-cracking stage when the surrounding SHLC^3 is damaged. However, $E_2{}^f$ values are consistently higher than that of the bare impregnated yarns, indicating that the short fibres contribute to the stiffness of the cracked composite. Indeed, the matrix is activated by crack bridging throughout the entire stress history of the hybrid specimen until failure, and very fine and close cracks form, which create a capillary pattern compared to conventional TRC, where net and well-spaced cracks trigger [65]. These observations nicely align with the findings of Gong et al. [18] and Zhu et al. [7], in antithesis to what is usually found in the literature for TRC, where the cracked matrix no longer contributes and the post-cracking modulus plainly mirrors that of the bare yarns [66,67]. The contribution to the stiffness of the hybrid composites turns out to be the highest for the system featuring the highest chemical affinity (i.e. C-MCF), with 8.6 % stiffening. This finding is consistent with previous studies that directly tally crack spacing and post-cracking stiffness with the quality of the textile-matrix bond [68], pointing out the role of the matrix and the interfacial interaction, especially for pseudo-ductile inorganic composites [69].

3.3.2.2. Ultimate state properties. To better illustrate the mechanical response of the three sets of composites at the ultimate state, mean values for strength and strain capacity are plotted in Fig. 17. TR-SHLC^3 including G-MCF yarns slightly outperforms C-MCF in terms of strength and strain capacity by 4.6 % and 7.7 %, respectively.

When textile-matrix bond is sufficient and the monolithic behaviour of the yarn is ensured, failure is ultimately governed by the tensile tolerance of the yarns and is independent of the bond [5,70,71]. Although bare G-MCF yarns exhibit a slightly lower mean strength than their C-MCF counterparts, frictional damage to the low grade cement suspension may have compromised the integrity of the carbon filaments at rupture. As expected, the TR-SHLC^3 samples containing the commercial epoxy-impregnated textiles feature the highest strength than the mineral-impregnated counterparts, aligned with the tensile strength of the bare yarns. The robustness of the performance indices is ascertained by a coefficient of variation (CoV) of less than 5 % for TR-SHLC^3 including mineral-impregnated textiles and between 6 % and 8 % for samples including epoxy-impregnated textiles.

To estimate the contribution of the fibre-reinforced matrix to the ultimate tensile performance of the TR-SHLC^3 hybrid composites (σ_{SHLC^3}), the peak load for each specimen is normalised to the area of the warp yarns of the textiles (A_f) and the average tensile strength of the bare yarns (f_{ftm}) is subtracted. This extra stress is then factorised with the reinforcement ratio of the textile, to account for the contribution provided by the entire SHLC^3 cross section (see Equation (3)).

$$\sigma_{SHLC^3} = \left(\frac{P_{max}}{A_f} - f_{ftm}\right)\rho_f \tag{3}$$

The additional contribution of the fibre-reinforced matrix is then plotted in Fig. 18, compared with the ultimate strength interval obtained on the

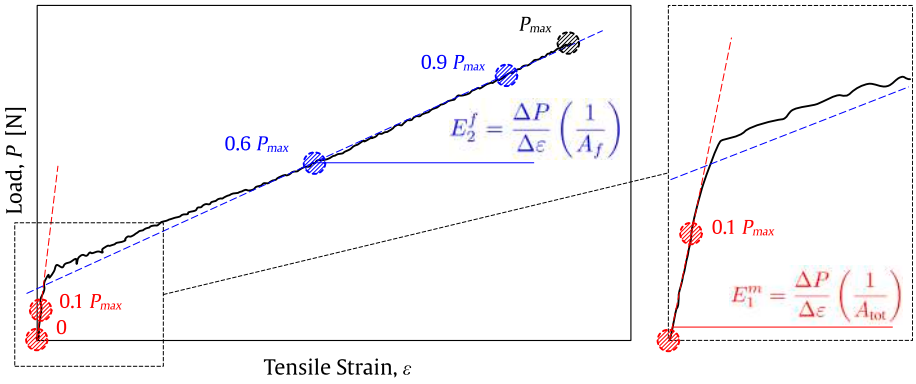

Fig. 15. Schematic representation of the calculation of the uncracked and post-cracking moduli of the TR-SHLC^3 plates, starting from a typical experimental tensile load–strain curve.

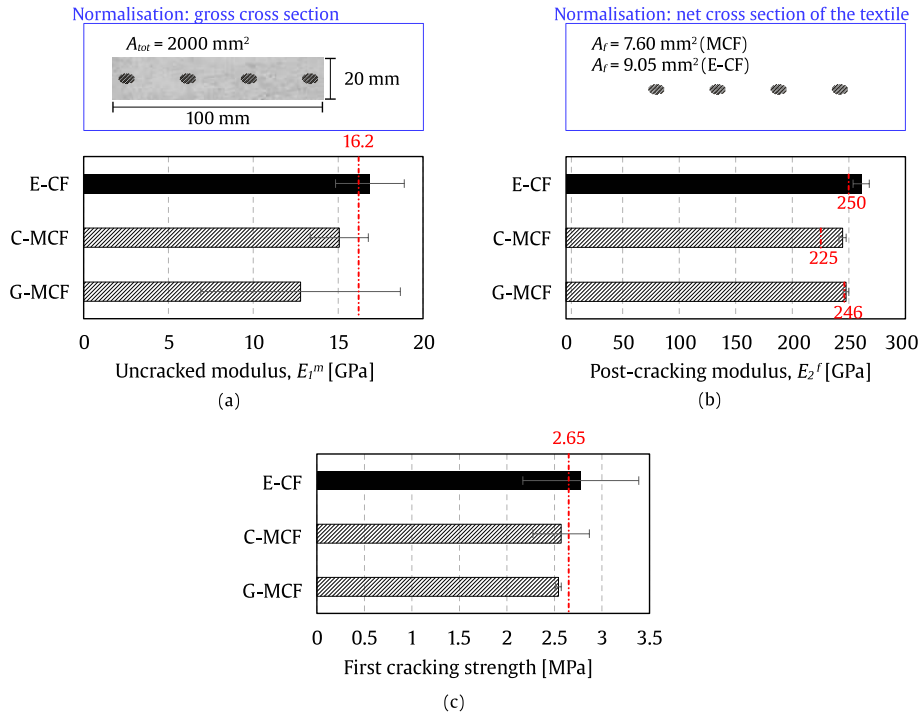

Fig. 16. Moduli at the uncracked and post-cracking stages as well as first cracking strength for different TR-SHLC^3 groups. The red dash-dotted lines represent the mean value for the plain SHLC^3 in the inlet (a) and the mean modulus of the different yarns, as reported in Table 1, in the inlet (b). Please note the different normalisation between the uncracked (E_1^m) and the post-cracking ($E_1{}^f$) moduli (see Equations (2). (For interpretation of the references to colour in this figure legend, the reader is referred to the web version of this article.)

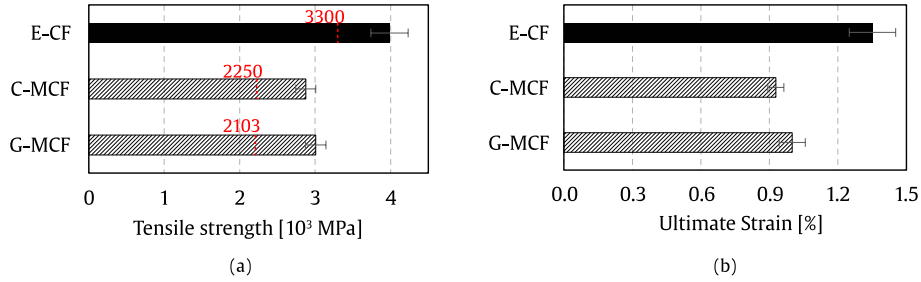

Fig. 17. Ultimate strength and strain mean values for different TR-SHLC^3 groups. Ultimate strength is normalised to the actual dry fibre cross-section. In red colour the mean tensile strength of the bare yarns is plotted. (For interpretation of the references to colour in this figure legend, the reader is referred to the web version of this article.)

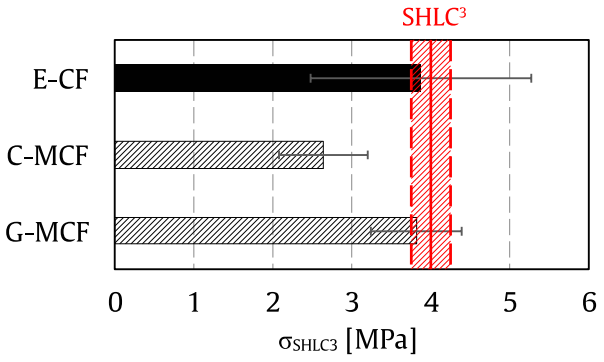

Fig. 18. Contribution to strength provided by the fibre-reinforced matrix (according to Equation (3)), compared to the tensile strength of the SHLC^3 matrix independently measured through tensile tests (Fig. 13).

SHLC^3 matrix (Fig. 13).

A comparison of these values with the tensile strength of the SHLC^3 matrix shows that for E-CF and G-MCF the additional load bearing capacity is close to the strength of the bare SHLC^3 matrix. This suggests that the external loads are effectively spread across the textile and the bridging fibres and the mechanical performance of the hybrid composite is maximised as the strength of both the textile and the SHLC^3 is attained at failure. On the contrary, the TR-SHLC^3 samples with C-MCF exhibit an average additional strength that is about 37 % lower than that of the SHLC^3. It is reasonable to assume that this may be a result of the finer cracks being arranged in a more capillary pattern due to the improved textile-matrix bond (see following section for *crack analysis*). As a consequence, when the textile attains its tensile strength, the short PE fibres are still effectively bridging all the cracks. In any case, the energy release due to textile failure is abrupt enough to cause the specimen to fail. However, further research is needed to confirm this hypothesis and more refined micromechanical studies are required, although the relationship between the development of more and finer cracks with a higher bridging capacity is understood to some extent [72]. This

correlation, though, is affected by several uncertainties including the inconsistency of crack widths, the scatter in the determination of the ultimate strength of the yarns, as well as the variability in fibre content and distribution due to the manufacturing process.

3.3.3. Crack analysis and connection with interface properties

Fig. 19 plots the average number of cracks and their average width in the vicinity of the peak load. Interestingly, the C-MCF specimens show pronounced cracking diffusion when compared to the G-MCF counterpart. In fact, the number of cracks at failure is 29 % higher, associated with a moderate reduction in the crack width of 9 %.

The appearance of the different crack patterns is comparable at three different test stages in the inlets of Fig. 20, where the axial strain values calculated by DIC analysis are mapped on the surface of the composite plate.

As a rule, the cracking behaviour of textile-reinforced cementitious composites is insensitive to the strength of the yarns, as it occurs mainly in the early stages of the loading history, and is rather indicative of the quality of the textile-matrix bond. Indeed, the superior quality of the chemical bond established at the interphase of the C-MCF, which is amply demonstrated by microscopic examination (see, e.g., the denser ITZ in Fig. 9) and by pull-out tests (see Fig. 10), results in the formation of a capillary and entangled crack structure. In addition to promoting an effective reinforcement for existing structures, these crack patterns are extremely beneficial as the protective layers effectively act as an effective barrier against chloride ingress and carbonation even under severe service conditions. Both TR-SHLC^3 composites including mineral-impregnated textiles attain an average crack width well below the 100 μm threshold, often invoked in design guidelines to limit the penetration of aggressive agents into the core of the structural members [73]. TR-SHLC^3 including epoxy-impregnated textiles displays a different crack pattern when compared to MCF counterparts. In fact, the cracks are mostly transverse, uniformly spaced, and less prone to branching and interconnection. This results in a more pronounced opening of the cracks at each stage of the loading history of the plate, reaching a mean value of around 100 μm at failure, which is still a reasonable extent for their use in the practice.

4. Conclusion

This paper investigates the tensile behaviour and crack control potential of novel classes of hybrid mineral-bonded composite materials. In particular, this study focuses on strain-hardening (SH) composites based on a high-performance limestone calcined clay cement (LC^3) binder containing short polyethylene fibres in combination with mineral-impregnated carbon fibre (MCF) textiles obtained by an automated impregnation and forming process. The effects of two different impregnating suspensions, namely metakaolin-based geopolymer (G) and cementitious (C) systems, are investigated in terms of bonding to the surrounding SHLC^3 matrix and of tensile behaviour. Homologous hybrid composites, including a commercially available epoxy impregnated textile, are also screened for comparative purposes. Based on the experimental evidence, the following observations can be made:

- Mineral-impregnated yarns produced by automated impregnation and forming techniques are successfully assembled into balanced biaxial textiles as continuous reinforcement for composite systems suitable for retrofitting to existing structures.
- Due to the high chemical affinity to LC^3 binders, cementitious impregnation results in a remarkable bond to the surrounding matrix compared to geopolymer counterpart, resulting in distinctive pull-out strength and chemical debonding energy values. This leads to fine and diffuse crack patterns in tensile tests with remarkable implications for serviceability. On the contrary, the purely frictional bond in E-CF composites leads to significantly wider cracks than in mineral-impregnated counterparts, resulting in lower efficiency against aggressive agent migration through the reinforced structure.
- The ultimate tensile performance of hybrid composites is mainly governed by the intrinsic properties (strength and ductility) of the carbon yarns, with very limited variation in the data due to the consistent occurrence of yarn tensile rupture as the failure mode and to the pseudo-ductile nature of the embedding SHLC^3 composite matrix imparted by the dispersed fibres.
- Unlike conventional TRC with brittle matrices, the addition of short fibres in the hybrid system ensures the active contribution of the matrix over the entire stress history of the composite through effective crack bridging, contributing positively to stiffness and strength.

In the light of the outcome of the present study, hybrid composite systems with mineral-impregnated yarns and short fibres emerge as attractive options as thin externally bonded protective layers to improve the service life and structural safety of buildings, in virtue of their remarkable energy absorption capacity combined with high tensile strength and pronounced thermal stability ensured by the inorganic nature of the impregnating agent. Although mineral impregnation is not yet able to ensure the same fibre alignment, consistency and ultimate performance as epoxy impregnations, the superior interphase bond promoted by mineral impregnation (particularly with the cementitious suspension) results in substantially improved control of crack opening, delivering significant advantages in terms of durability under service conditions compared to conventional epoxy impregnation. In addition, the continuous development and fine-tuning of more sustainable binders and impregnating agents for multifilament yarns, by reducing the amount of Portland clinker, is also a key milestone in minimising the carbon footprint and CO_2 emissions of the built environment.

CRediT authorship contribution statement

Cesare Signorini: Writing – review & editing, Writing – original draft, Visualization, Validation, Project administration, Methodology, Investigation, Formal analysis, Data curation, Conceptualization. **Ameer H. Ahmed:** Formal analysis, Investigation, Visualization. **Marco Liebscher:** Writing – review & editing, Validation, Resources,

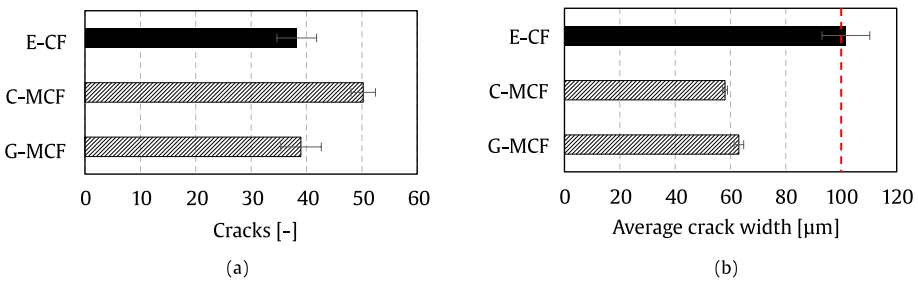

Fig. 19. Crack average number and width for different TR-SHLC^3 groups. The dashed line at 100 μm refers to the threshold for crack opening width recommended by guidelines over the service time of cementitious structural elements.

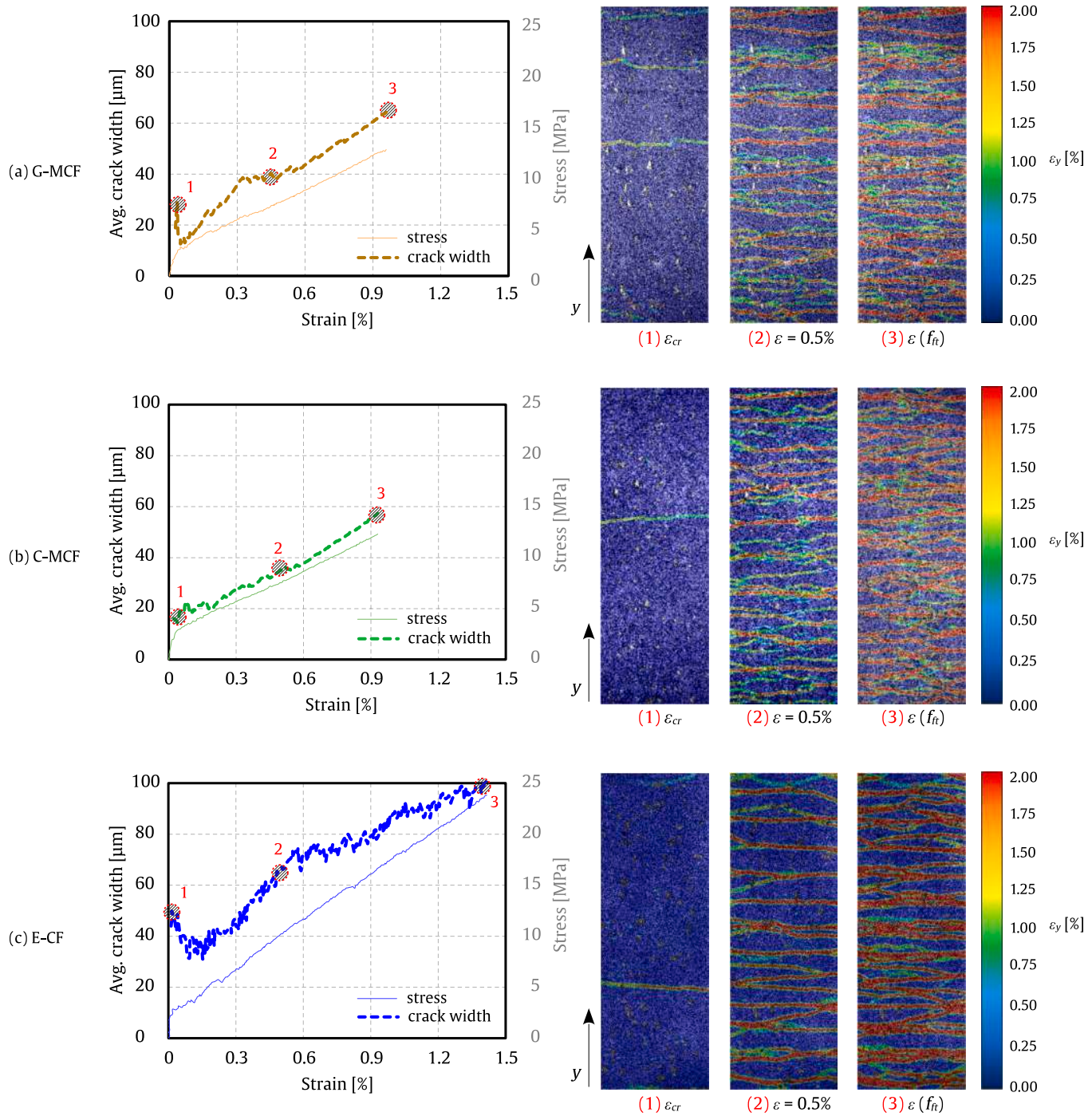

Fig. 20. Axial strain colour map documenting the crack patterns for TR-SHLC[3] representative specimens at three different strain levels. The charts on the left show the evolution of the average crack width during the test (the crack width is shown as a dashed line on the primary axis, while the corresponding stress–strain curve is shown as a solid line on the secondary axis).

Methodology, Conceptualization. **Jitong Zhao:** Investigation, Formal analysis. **Thomas Köberle:** Investigation, Formal analysis. **Viktor Mechtcherine:** Writing – review & editing, Validation, Supervision, Resources, Funding acquisition.

Declaration of competing interest

The authors declare that they have no known competing financial interests or personal relationships that could have appeared to influence the work reported in this paper.

Acknowledgment

Funding: The financial support of the German Research Foundation (Deutsche Forschungsgemeinschaft, DFG) in the framework of the Research Training Group (Graduiertenkollegs, GRK) 2250, entitled "*Mineral-bonded composites for enhanced structural impact safety*" (grant nr. 287321140) is gratefully acknowledged. The authors are also grateful for the support provided by Mr Kai-Uwe Mehlisch in the mechanical testing phase.

Data availability

Data will be made available on request.

References

[1] V.C. Li, On Engineered Cementitious Composites (ECC), J. Adv. Concr. Technol. 1 (2003) 215–230, https://doi.org/10.3151/JACT.1.215.

[2] T.C.S.P. Figueiredo, I. Curosu, G.L.G. Gonzáles, M. Hering, F.D.A. Silva, M. Curbach, V. Mechtcherine, Mechanical behavior of strain-hardening cement-based composites (SHCC) subjected to torsional loading and to combined torsional and axial loading, Mater. Des. 198 (2021) 109371, https://doi.org/10.1016/j.matdes.2020.109371.

[3] K.-Q. Yu, J.-G. Dai, Z.-D. Lu, C.-S. Poon, Rate-dependent tensile properties of ultra-high performance engineered cementitious composites (UHP-ECC), Cem. Concr. Compos. 93 (2018) 218–234, https://doi.org/10.1016/j.cemconcomp.2018.07.016.

[4] K. Yu, Y. Ding, J. Liu, Y. Bai, Energy dissipation characteristics of all-grade polyethylene fiber-reinforced engineered cementitious composites (PE-ECC), Cem. Concr. Compos. 106 (2020) 103459, https://doi.org/10.1016/j.cemconcomp.2019.103459.

[5] R. Barhum, V. Mechtcherine, Effect of short, dispersed glass and carbon fibres on the behaviour of textile-reinforced concrete under tensile loading, Eng. Fract. Mech. 92 (2012) 56–71, https://doi.org/10.1016/j.engfracmech.2012.06.001.

[6] R. Barhum, V. Mechtcherine, Influence of short dispersed and short integral glass fibres on the mechanical behaviour of textile-reinforced concrete, Mater. Struct. 46 (2013) 557–572, https://doi.org/10.1617/s11527-012-9913-3.

[7] D. Zhu, S. Liu, Y. Yao, G. Li, Y. Du, C. Shi, Effects of short fiber and pre-tension on the tensile behavior of basalt textile reinforced concrete, Cem. Concr. Compos. 96 (2019) 33–45, https://doi.org/10.1016/j.cemconcomp.2018.11.015.

[8] M. Alma'aitah, B. Ghiassi, B. Mobasher, F. Kanavaris, Synergising hybrid short fibres and composite cements for sustainable and efficient textile-reinforced concrete composites, Journal of Building Engineering 93 (2024) 109857. https://doi.org/10.1016/j.jobe.2024.109857.

[9] C. Signorini, F. Bracklow, M. Hering, M. Butler, L. Leicht, T. Schubert, M.A. B. Beigh, B. Beckmann, M. Curbach, V. Mechtcherine, Ballistic limit and damage assessment of hybrid fibre-reinforced cementitious thin composite plates under impact loading, Journal of Building Engineering 80 (2023) 108037, https://doi.org/10.1016/j.jobe.2023.108037.

[10] C. Signorini, A. Nobili, Comparing durability of steel reinforced grout (SRG) and textile reinforced mortar (TRM) for structural retrofitting, Mater. Struct. 54 (2021) 1–15, https://doi.org/10.1617/s11527-021-01729-3.

[11] I. Curosu, M. Liebscher, S. Burk, H. Li, S. Hempel, N. Raak, H. Rohm, V. Mechtcherine, Influence of fiber type on the tensile behavior of high-strength strain-hardening cement-based composites (SHCC) at elevated temperatures, Mater. Des. 198 (2021) 109397, https://doi.org/10.1016/j.matdes.2020.109397.

[12] Q. Zhang, S. Li, S. Gong, G. Zhang, G. Xi, Y. Wu, Study on flexural properties of basalt fiber textile reinforced concrete (BTRC) sheets including short AR-glass fibers, Front. Mater. 7 (2020) 277, https://doi.org/10.3389/fmats.2020.00277.

[13] P. Böer, L. Holliday, T.H.K. Kang, Independent environmental effects on durability of fiber-reinforced polymer wraps in civil applications: a review, Constr. Build. Mater. 48 (2013) 360–370, https://doi.org/10.1016/j.conbuildmat.2013.06.077.

[14] F. de Andrade Silva, M. Butler, S. Hempel, R.D. Toledo Filho, V. Mechtcherine, F. de A. Silva, M. Butler, S. Hempel, R.D. Toledo Filho, V. Mechtcherine, Effects of elevated temperatures on the interface properties of carbon textile-reinforced concrete, Cement and Concrete Composites 48 (2014) 26–34. https://doi.org/10.1016/J.CEMCONCOMP.2014.01.007.

[15] C. Scheffler, S.L. Gao, R. Plonka, E. Mäder, S. Hempel, M. Butler, V. Mechtcherine, Interphase modification of alkali-resistant glass fibres and carbon fibres for textile reinforced concrete I: Fibre properties and durability, Compos. Sci. Technol. 69 (2009) 531–538, https://doi.org/10.1016/j.compscitech.2008.11.027.

[16] B.A. Newcomb, Processing, structure, and properties of carbon fibers, Compos. A Appl. Sci. Manuf. 91 (2016) 262–282, https://doi.org/10.1016/j.compositesa.2016.10.018.

[17] J. Donnini, V. Corinaldesi, A. Nanni, Mechanical properties of FRCM using carbon fabrics with different coating treatments, Compos. B Eng. 88 (2016) 220–228, https://doi.org/10.1016/j.compositesb.2015.11.012.

[18] T. Gong, A.H. Ahmed, I. Curosu, V. Mechtcherine, Tensile behavior of hybrid fiber reinforced composites made of strain-hardening cement-based composites (SHCC) and carbon textile, Constr. Build. Mater. 262 (2020) 120913, https://doi.org/10.1016/j.conbuildmat.2020.120913.

[19] S. Guo, J. Ren, T. Yang, M.Z. Rahman, C. Shi, D. Zhu, Influences of surface treatment on the mechanical performances of carbon and basalt textiles-reinforced concretes under harsh environments, Compos. B Eng. 246 (2022) 110195, https://doi.org/10.1016/j.compositesb.2022.110195.

[20] C. Signorini, A. Sola, A. Nobili, Hierarchical composite coating for enhancing the tensile behaviour of textile-reinforced mortar (TRM), Cem. Concr. Compos. 140 (2023) 105082, https://doi.org/10.1016/j.cemconcomp.2023.105082.

[21] M. Messori, A. Nobili, C. Signorini, A. Sola, Effect of high temperature exposure on epoxy-coated glass textile reinforced mortar (GTRM) composites, Constr. Build. Mater. 212 (2019) 765–774, https://doi.org/10.1016/j.conbuildmat.2019.04.026.

[22] J. Zhao, A.H. Ahmed, M. Liebscher, A. Bartsch, E. Ivaniuk, M. Butler, J. Kohout, P. Hájková, V. Mechtcherine, Thermomechanical behavior of textile-reinforced geopolymer concrete based on mineral-impregnated carbon-fibers (MCFs) composites, Cem. Concr. Compos. 150 (2024) 105555, https://doi.org/10.1016/j.cemconcomp.2024.105555.

[23] J. Zhao, C. Signorini, A. Nobili, M. Liebscher, J. Kohout, P. Hájková, V. Mechtcherine, Experimental and analytical analysis of the bond alteration of impregnated carbon fibre reinforcements embedded in alkali-activated concrete at elevated temperatures, Constr. Build. Mater. 435 (2024) 136794, https://doi.org/10.1016/j.conbuildmat.2024.136794.

[24] V. Bertolli, C. Signorini, A. Nobili, T. D'Antino, Influence of severe thermal preconditioning on the bond between carbon FRCM and masonry substrate: effect of textile pre-impregnation, Constr. Build. Mater. 409 (2023) 134028, https://doi.org/10.1016/j.conbuildmat.2023.134028.

[25] R.M. de C. Silva, J. Zhao, M. Liebscher, I. Curosu, F. de A. Silva, V. Mechtcherine, Bond behavior of polymer- and mineral-impregnated carbon fiber yarns towards concrete matrices at elevated temperature levels, Cement and Concrete Composites 133 (2022) 104685. https://doi.org/10.1016/j.cemconcomp.2022.104685.

[26] Z. Cohen, A. Peled, Effect of nanofillers and production methods to control the interfacial characteristics of glass bundles in textile fabric cement-based composites, Compos. A Appl. Sci. Manuf. 43 (2012) 962–972, https://doi.org/10.1016/j.compositesa.2012.01.022.

[27] R. Nadiv, A. Peled, V. Mechtcherine, S. Hempel, C. Schroefl, Micro- and nanoparticle mineral coating for enhanced properties of carbon multifilament yarn cement-based composites, Compos. B Eng. 111 (2017) 179–189, https://doi.org/10.1016/j.compositesb.2016.12.005.

[28] C. Signorini, A. Nobili, Targeting functionalised carbon nanotubes at the interphase of Textile Reinforced Mortar (TRM) composites, Compos. A Appl. Sci. Manuf. 144 (2021) 106330, https://doi.org/10.1016/j.compositesa.2021.106330.

[29] J. Zhao, M. Liebscher, T. Köberle, A. Almanla, V. Mechtcherine, Mineral-impregnated carbon-fiber (MCF) composites made with differently sized fly-ash geopolymers for durable light weight and high temperature applications, Cem. Concr. Compos. 138 (2023) 104950, https://doi.org/10.1016/j.cemconcomp.2023.104950.

[30] K. Schneider, M. Lieboldt, M. Liebscher, M. Fröhlich, S. Hempel, M. Butler, C. Schröfl, V. Mechtcherine, Mineral-based coating of plasma-treated carbon fibre rovings for carbon concrete composites with enhanced mechanical performance, Materials 10 (2017) 360, https://doi.org/10.3390/ma10040360.

[31] M. Liebscher, J. Zhao, G. Wilms, A. Michel, K. Wilhelm, V. Mechtcherine, Influence of roller configuration on the fiber–matrix distribution and mechanical properties of continuously produced, mineral-impregnated carbon fibers (MCFs), Fibers 10 (2022) 42, https://doi.org/10.3390/fib10050042.

[32] B. Banholzer, T. Brockmann, W. Brameshuber, Material and bonding characteristics for dimensioning and modelling of textile reinforced concrete (TRC) elements, Mater. Struct. 39 (2006) 749–763.

[33] K. Schneider, A. Michel, M. Liebscher, L. Terreri, S. Hempel, V. Mechtcherine, Mineral-impregnated carbon fibre reinforcement for high temperature resistance of thin-walled concrete structures, Cem. Concr. Compos. 97 (2019) 68–77, https://doi.org/10.1016/j.cemconcomp.2018.12.006.

[34] V. Mechtcherine, R. Buswell, H. Kloft, F.P. Bos, N. Hack, R. Wolfs, J. Sanjayan, B. Nematollahi, E. Ivaniuk, T. Neef, Integrating reinforcement in digital fabrication with concrete: a review and classification framework, Cem. Concr. Compos. 119 (2021) 103964, https://doi.org/10.1016/j.cemconcomp.2021.103964.

[35] B.C. McLellan, R.P. Williams, J. Lay, A. van Riessen, G.D. Corder, Costs and carbon emissions for geopolymer pastes in comparison to ordinary portland cement, J. Clean. Prod. 19 (2011) 1080–1090, https://doi.org/10.1016/j.jclepro.2011.02.010.

[36] S. Cholostiakow, L.N. Koutas, C.G. Papakonstantinou, Geopolymer versus cement-based textile-reinforced mortar: Diagonal compression tests on masonry walls representative of infills in RC frames, Constr. Build. Mater. 373 (2023) 130836, https://doi.org/10.1016/j.conbuildmat.2023.130836.

[37] S.M. Laskar, S. Talukdar, Preparation and tests for workability, compressive and bond strength of ultra-fine slag based geopolymer as concrete repairing agent, Constr. Build. Mater. 154 (2017) 176–190, https://doi.org/10.1016/j.conbuildmat.2017.07.187.

[38] L. Wang, Z. Zhu, A. Hamza Ahmed, M. Liebscher, X. Zhu, V. Mechtcherine, Self-healing behavior of high-strength strain-hardening cement-based composites (HS-SHCC) blended with limestone calcined clay cement (LC3), Construction and Building Materials 370 (2023) 130633. https://doi.org/10.1016/j.conbuildmat.2023.130633.

[39] J. Zhao, M. Liebscher, A. Michel, D. Junger, A.C.C. Trindade, F. de Andrade Silva, V. Mechtcherine, Development and testing of fast curing, mineral-impregnated carbon fiber (MCF) reinforcements based on metakaolin-made geopolymers, Cement and Concrete Composites 116 (2021) 103898, https://doi.org/10.1016/j.cemconcomp.2020.103898.

[40] K. Scrivener, F. Martirena, S. Bishnoi, S. Maity, Calcined clay limestone cements (LC3), Cem. Concr. Res. 114 (2018) 49–56, https://doi.org/10.1016/j.cemconres.2017.08.017.

[41] Dyneema® Fact Sheets, (2010). https://issuu.com/eurofibers/docs/name8f0d44 (accessed March 15, 2023).

[42] J. Hartig, F. Jesse, K. Schicktanz, U. Häußler-Combe, Influence of experimental setups on the apparent uniaxial tensile load-bearing capacity of Textile Reinforced Concrete specimens, Materials and Structures/materiaux et Constructions 45 (2012) 433–446, https://doi.org/10.1617/s11527-011-9775-0.

[43] RILEM 232-TDT, Test methods and design of textile reinforced concrete, 2016. https://doi.org/10.1617/s11527-016-0839-z.

[44] F. Nerilli, B. Ferracuti, A tension stiffening model for FRCM reinforcements calibrated by means of an extended database, Compos. Struct. 284 (2022) 115100, https://doi.org/10.1016/j.compstruct.2021.115100.

[45] S. Han, P. Yan, X. Kong, Study on the compatibility of cement-superplasticizer system based on the amount of free solution, Sci. China Technol. Sci. 54 (2011) 183–189, https://doi.org/10.1007/s11431-010-4174-2.
[46] J. Zhao, M. Liebscher, L. Tzounis, V. Mechtcherine, Role of sizing agent on the microstructure morphology and mechanical properties of mineral-impregnated carbon-fiber (MCF) reinforcement made with geopolymers, Appl. Surf. Sci. 567 (2021) 150740, https://doi.org/10.1016/j.apsusc.2021.150740.
[47] Y.-S. Wang, K.-D. Peng, Y. Alrefaei, J.-G. Dai, The bond between geopolymer repair mortars and OPC concrete substrate: Strength and microscopic interactions, Cem. Concr. Compos. 119 (2021) 103991, https://doi.org/10.1016/j.cemconcomp.2021.103991.
[48] W. Kong, Y. Wei, S. Wang, J. Chen, Y. Wang, Research progress on cement-based materials by X-ray computed tomography, Int. J. Pavement Res. Technol. 13 (2020) 366–375, https://doi.org/10.1007/s42947-020-0119-8.
[49] C. Signorini, A. Sola, B. Malchiodi, A. Nobili, Highly dissipative fiber-reinforced concrete for structural screeds, J. Mater. Civ. Eng. 34 (2022) 04022022, https://doi.org/10.1061/(ASCE)MT.1943-5533.0004160.
[50] C. Signorini, A. Nobili, M. Liebscher, J. Zhao, A.H. Ahmed, T. Köberle, V. Mechtcherine, Assessing the stress-transfer capability of mineral impregnated PBO yarns in a limestone calcined clay cement-based (LC3) matrix, Compos. B Eng. 276 (2024) 111364, https://doi.org/10.1016/j.compositesb.2024.111364.
[51] A. Peled, E. Zaguri, G. Marom, Bonding characteristics of multifilament polymer yarns and cement matrices, Compos. A Appl. Sci. Manuf. 39 (2008) 930–939, https://doi.org/10.1016/j.compositesa.2008.03.012.
[52] Z. Lin, T. Kanda, V.C. Li, On interface property characterization and performance of fiber reinforced cementitious composites, Concr. Sci. Eng. 1 (1999) 173–184.
[53] M. Konrad, R. Chudoba, The influence of disorder in multifilament yarns on the bond performance in textile reinforced concrete, Acta Polytech 44 (2004). https://doi.org/10.14311/654.
[54] H. Li, M. Liebscher, A. Michel, A. Quade, R. Foest, V. Mechtcherine, Oxygen plasma modification of carbon fiber rovings for enhanced interaction toward mineral-based impregnation materials and concrete matrices, Constr. Build. Mater. 273 (2021) 121950, https://doi.org/10.1016/j.conbuildmat.2020.121950.
[55] ACI PRC-549.4-20, Guide to Design and Construction of Externally Bonded Fabric-Reinforced and Steel-Reinforced Grout Systems for Repair and Strengthening of Concrete Structures, American Concrete Institute, 2020.
[56] M. El Kadi, P. Kapsalis, D. Van Hemelrijck, J. Wastiels, T. Tysmans, Influence of loading orientation and knitted versus woven transversal connections in 3D textile reinforced cement (TRC) composites, Appl. Sci. 10 (2020) 4517, https://doi.org/10.3390/app10134517.
[57] D. De Domenico, N. Maugeri, P. Longo, G. Ricciardi, G. Gullì, L. Calabrese, Clevis-grip tensile tests on basalt, carbon and steel FRCM systems realized with customized cement-based matrices, J. Compos. Sci. 6 (2022) 275, https://doi.org/10.3390/jcs6090275.
[58] S. De Santis, H.A. Hadad, F. De Caso y Basalo, G. de Felice, A. Nanni, Acceptance criteria for tensile characterization of fabric-reinforced cementitious matrix systems for concrete and masonry repair, J. Compos. Constr. 22 (2018) 04018048. https://doi.org/10.1061/(ASCE)CC.1943-5614.0000886.
[59] D. Arboleda, F.G. Carozzi, A. Nanni, C. Poggi, Testing procedures for the uniaxial tensile characterization of fabric-reinforced cementitious matrix composites, J. Compos. Constr. 20 (2016) 04015063, https://doi.org/10.1061/(ASCE)CC.1943-5614.0000626.
[60] M. Butler, V. Mechtcherine, S. Hempel, Durability of textile reinforced concrete made with AR glass fibre: effect of the matrix composition, Mater. Struct. 43 (2010) 1351–1368.
[61] ICC AC434, Acceptance criteria for masonry and concrete strengthening using fiber-reinforced cementitious matrix (FRCM) composite systems, 2018.
[62] D. Arboleda, S. Babaeidarabad, C.D.L. Hays, A. Nanni, Durability of Fabric Reinforced Cementitious Matrix (FRCM). Composites, in: International Institute for FRP in Construction (IIFC), 2014.
[63] C. Signorini, A. Nobili, F.O. Falope, Mechanical performance and crack pattern analysis of aged Carbon Fabric Cementitious Matrix (CFRCM) composites, Compos. Struct. (2018), https://doi.org/10.1016/j.compstruct.2018.05.052.
[64] A.H. Ahmed, M. Liebscher, V. Mechtcherine, Mechanical performance of strain hardening limestone calcined clay cementitious composites (SHLC4) subject to wet-dry cycles, in: M. Kunieda, T. Kanakubo, T. Kanda, K. Kobayashi (Eds.), Strain Hardening Cementitious Composites, Springer International Publishing, Cham, 2023: pp. 3–12. https://doi.org/10.1007/978-3-031-15805-6_1.
[65] Y. Yao, A. Bonakdar, J. Faber, T. Gries, B. Mobasher, Distributed cracking mechanisms in textile-reinforced concrete under high speed tensile tests, Mater. Struct. 49 (2016) 2781–2798, https://doi.org/10.1617/s11527-015-0685-4.
[66] V.D. Truong, D.J. Kim, A review paper on direct tensile behavior and test methods of textile reinforced cementitious composites, Compos. Struct. 263 (2021) 113661, https://doi.org/10.1016/j.compstruct.2021.113661.
[67] A. Nobili, Durability assessment of impregnated Glass Fabric Reinforced Cementitious Matrix (GFRCM) composites in the alkaline and saline environments, Constr. Build. Mater. 105 (2016) 465–471, https://doi.org/10.1016/j.conbuildmat.2015.12.173.
[68] D.A.S. Rambo, Y. Yao, F. de Andrade Silva, R.D. Toledo Filho, B. Mobasher, Experimental investigation and modelling of the temperature effects on the tensile behavior of textile reinforced refractory concretes, Cem. Concr. Compos. 75 (2017) 51–61, https://doi.org/10.1016/j.cemconcomp.2016.11.003.
[69] O.A. Cevallos, R.S. Olivito, Effects of fabric parameters on the tensile behaviour of sustainable cementitious composites, Compos. B Eng. 69 (2015) 256–266, https://doi.org/10.1016/j.compositesb.2014.10.004.
[70] S. De Santis, F.G. Carozzi, G. de Felice, C. Poggi, Test methods for textile reinforced mortar systems, Compos. B Eng. 127 (2017) 121–132, https://doi.org/10.1016/j.compositesb.2017.03.016.
[71] F.G. Carozzi, A. Bellini, T. D'Antino, G. de Felice, F. Focacci, Ł. Hojdys, L. Laghi, E. Lanoye, F. Micelli, M. Panizza, C. Poggi, Experimental investigation of tensile and bond properties of Carbon-FRCM composites for strengthening masonry elements, Compos. B Eng. 128 (2017) 100–119, https://doi.org/10.1016/j.compositesb.2017.06.018.
[72] X. Zheng, J. Zhang, Z. Wang, Effect of multiple matrix cracking on crack bridging of fiber reinforced engineered cementitious composite, J. Compos. Mater. 54 (2020) 3949–3965, https://doi.org/10.1177/0021998320923145.
[73] M. Basteskår, M. Engen, T. Kanstad, K.T. Fosså, A review of literature and code requirements for the crack width limitations for design of concrete structures in serviceability limit states, Struct. Concr. 20 (2019) 678–688, https://doi.org/10.1002/suco.201800183.